Long-term global ocean heat content change driven by sub-polar surface heat fluxes

Taimoor Sohail[1], Damien B. Irving[2], Jan D. Zika[1], Ryan M. Holmes[1,2,3] and John A. Church[2]

[1]School of Mathematics and Statistics, University of New South Wales, Sydney, Australia
[2]Climate Change Research Centre, University of New South Wales, Sydney, Australia
[3]ARC Centre of Excellence for Climate Extremes, University of New South Wales, Sydney, Australia

Key Points:

- We introduce a novel tracer-percentile framework which relates ocean heat content trends to surface flux and turbulent mixing changes
- Heat content changes in the 90% coldest ocean volume are traced to heat fluxes which, on average, enter 23% of the surface area of the ocean
- Using this framework, we trace a cooling bias in the 5-20% warmest volume of CMIP6 climate models to surface flux biases

Corresponding author: Taimoor Sohail, t.sohail@unsw.edu.au

Abstract

The ocean has absorbed approximately 90% of the accumulated heat in the climate system since 1970. As global warming accelerates, understanding ocean heat content changes and tracing these to surface heat input is becoming increasingly important. We introduce a novel tracer-percentile framework in which we organise the ocean into temperature percentiles from warmest to coldest, allowing us to trace changes in ocean temperature to changes in air-sea heat fluxes and mixing. Applying this framework to observations and historical CMIP6 simulations, we find that 40% of heat uptake between 1970 and 2014 occurs in the warmest 10% ocean volume. However, the coolest 90% ocean volume outcrops over 23% of the ocean's surface area, implying a disproportionately large heat input per unit area. Additionally, a cold bias in the CMIP6 models is traced to inaccurate sea surface temperatures and surface heat fluxes into the warmest 5 – 20% ocean volume.

Plain Language Summary

The ocean has absorbed approximately 90% of the heat that has built up in the climate system since 1970. Understanding the processes which drive this uptake of heat by the ocean is critical to climate projections. Typically, this has required the use of climate and ocean models, which must be validated with ocean observations. To enable this, we introduce a new method, the tracer-percentile framework, which allows us to directly use observations to understand the processes dictating heat uptake by the ocean. Using climate models (collectively called CMIP6) and ocean observations, we calculate the heat input into layers of water at the ocean surface, the total heat stored in these layers, and the mixing of heat between these layers. We find that the heat input at the surface and heat stored in the ocean has increased between 1970 and 2014, with 60% of the increase in heat uptake at the surface happening over about a quarter of the ocean's surface, which connects to 90% of the world's ocean volume. We also identify inaccuracies in the CMIP6 models and trace these problems to the way the surface properties of the ocean (or surface heat input) are represented.

1 Introduction

The global ocean has absorbed approximately 90% of the excess heat in the climate system since 1970 [*Schuckmann et al.*, 2020], impacting global sea level rise [*Domingues et al.*, 2008; *Church and White*, 2011; *Gregory et al.*, 2013], surface air temperature [*Watanabe et al.*, 2013] and extreme weather [*Lin et al.*, 2013]. As the radiative imbalance of the planet is so difficult to measure directly, knowledge of global ocean heat content (OHC) changes resulting from ocean heat uptake is critical for monitoring climate change. Heat enters the ocean at the surface and is subsequently advected and diffused in the ocean [*Gregory*, 2000; *Kuhlbrodt et al.*, 2015; *Liang et al.*, 2015; *Cummins et al.*, 2016]. Past research has thus articulated a *fixed-depth framework*, which quantifies changes in global OHC at a given depth as a balance between surface fluxes and vertical advection and diffusion. Analysing ocean circulation and heat transport in fixed-depth coordinates has yielded a number of insights. Prior work has established that mean downward heat transport is balanced by along-isopycnal upward eddy fluxes, particularly in the Southern Ocean [*Gregory*, 2000; *Gnanadesikan et al.*, 2005; *Wolfe et al.*, 2008; *Morrison et al.*, 2013; *Kuhlbrodt et al.*, 2015]. In addition, *Zika et al.* [2013] found that downward heat transport in the meridional overturning circulation is driven by a combination of salinification in the subtropics and wind-driven Ekman pumping in the Southern Ocean.

While the fixed-depth framework provides a useful way of analysing heat transport, it can be challenging to *quantify* observed OHC, as this requires knowledge of the velocity field [something that is only possible with models (e.g., *Wolfe et al.* [2008]; *Kuhlbrodt*

et al. [2015]) and reanalysis products (e.g., *Liang et al.* [2015, 2017])]. Importantly, the vertical heat budget is impacted by adiabatic processes, internal variability and heave, meaning that adiabatic redistribution of existing heat impacts trends in OHC at fixed depth. Therefore, there remains scope to develop a framework which quantifies how much observed heat is added to the climate system at a given location.

Numerous studies have moved towards analysing ocean circulation and heat transport in a water mass-based reference frame [*Walin*, 1982; *Groeskamp et al.*, 2019]. Recently this framework has been used to understand climate change [*Zika et al.*, 2015] and climate variability [*Evans et al.*, 2017]. *Holmes et al.* [2019] formalised a heat budget in fixed-temperature coordinates, termed the diathermal heat transport framework. By analysing heat transport across a given *isotherm*, adiabatic processes, internal variability and heave are excluded. In the resulting *temperature-based framework*, heat content tendencies are tracked to changes in diabatic transport processes - air-sea fluxes and mixing [*Holmes et al.*, 2019]. The temperature-based framework allows us to link the temperature at which heat enters the ocean to the temperature classes which exhibit OHC changes. Diathermal fluxes may also be calculated purely from observed in-situ temperature and surface flux data (with the mixing term calculated by residual).

The temperature-based framework addresses the challenges posed by the fixed-depth framework, but also presents its own complications. For instance, isotherms shift as the ocean warms such that the characteristic isotherms of a given region move to a different region, making partitioning between the tropics, sub-tropics and sub-polar oceans difficult. We introduce a novel diagnostic which defines OHC changes at temperature percentiles, ordered from warmest to coldest. The new *tracer-percentile framework* allows us to quantify observed changes in OHC and trace them to changes in surface heat fluxes and mixing using a coarse-resolution hydrographic observational dataset. The tracer-percentile framework also enables a direct evaluation of model biases and attribution of biases to surface fluxes or mixing. In a uniformly warming ocean, the tracer-percentile framework avoids issues associated with shifting isotherms. In addition, organising the ocean by volume means that OHC changes can be translated into changes in the temperature of the surface that bounds a given volume percentile, allowing a comparison with changes in the globally-averaged temperature at fixed depth.

In section 2, we define the heat budget in terms of the tracer-percentile framework. In section 3, we summarise the data sources used in the analysis. In section 4, we detail the key results of the study, and in section 5 we summarise this work and discuss important implications.

2 Theory

2.1 The tracer-percentile framework

In the fixed-depth framework, the variable of interest is $H(z,t)$, the total OHC above a given depth z (equivalent to the volume-integral of the temperature multiplied by the reference density ρ_0 and specific heat capacity of seawater C_p, in the Boussinesq case). The fixed-temperature framework, on the other hand, considers the total OHC above a given isotherm $\mathcal{H}(\Theta^*,t)$ where the corresponding volume is denoted $\mathcal{V}(\Theta^*,t)$ [*Palmer and Haines*, 2009; *Holmes et al.*, 2019]:

$$\begin{aligned}\mathcal{V}(\Theta^*,t) &= \iiint_{\Theta(x,y,z,t)>\Theta^*} dxdydz;\\ \mathcal{H}(\Theta^*,t) &= \rho_0 C_p \int_0^{\mathcal{V}(\Theta^*,t)} \Theta(x,y,z,t)d\mathcal{V},\end{aligned} \tag{1}$$

where Θ is the three-dimensional temperature field and Θ^* is the binning temperature over which the integration occurs.

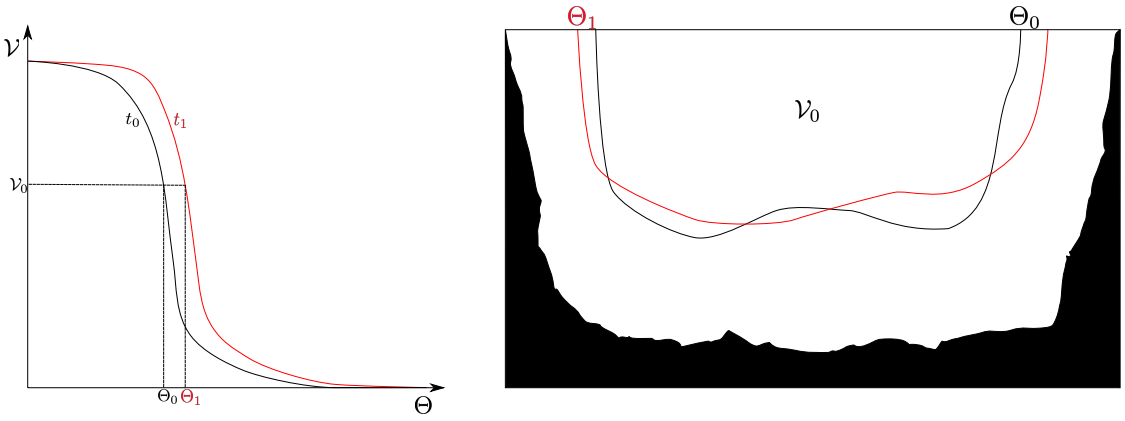

Figure 1. Illustration of the change in bounding temperature of a fixed volume in a warming ocean. *Left:* Cumulative distribution of volume as a function of temperature, ordered from hot to cold, at times t_0 (black) and t_1 (red), where t_1>t_0. *Right:* Zonally-averaged representation of the volume $\mathcal{V}_0$ and the bounding temperature $\Theta_0(\mathcal{V}_0, t_0)$ (black) and $\Theta_1(\mathcal{V}_0, t_1)$ (red).

The cumulative distribution function (CDF) of volume $\mathcal{V}(\Theta, t)$ in temperature coordinates (organised from warmest to coldest) is illustrated in figure 1 at times t_0 and t_1 (where the ocean is assumed to warm uniformly for illustrative purposes). As the ocean warms, assuming the thermal expansion of sea water negligibly modifies the total volume of the ocean, the CDF moves along the temperature axis while remaining fixed in the cumulative volume axis. Hence, at a fixed temperature the volume increases, and at a fixed volume the bounding temperature increases. In the *tracer-percentile framework*, we invert the volume equation in (1) to get the bounding tracer (in this case temperature) $\Theta^{\mathcal{V}}(\mathcal{V}, t)$ of a given volume $\mathcal{V}(\Theta, t)$:

$$\mathcal{V}(\Theta^*, t) \Longleftrightarrow \Theta^{\mathcal{V}}(\mathcal{V}, t), \tag{2}$$

The temperature-percentile is $p(\Theta^*, t) = 100 \times \mathcal{V}(\Theta^*, t)/\mathcal{V}_T$, where V_T is the total volume of the ocean. Note that we ignore the negligible changes in the total volume of the ocean with time. OHC in temperature percentiles is therefore expressed as:

$$\mathcal{H}(p, t) = 0.01 \mathcal{V}_T \rho_0 C_p \int_0^p \Theta^p(p, t) dp, \tag{3}$$

where $\Theta^p(p, t)$ is equivalent to $\Theta^{\mathcal{V}}(\mathcal{V}, t)$ at a given temperature-percentile.

2.2 Ocean heat content tendency

The OHC tendency in temperature percentiles, $\partial\mathcal{H}(p, t)/\partial t$, may be related to specific diabatic heat transport processes, providing insight into the drivers of OHC changes. To formulate the OHC tendency budget in temperature percentiles, we begin by looking at the diathermal heat transport budget introduced by *Holmes et al.* [2019] for the fixed-temperature framework.

In the fixed-temperature framework, the total heat content tendency $\partial\mathcal{H}(\Theta, t)/\partial t$ is a consequence of changes in the surface forcing $\mathcal{F}$, mixing $\mathcal{M}$ and diathermal heat ad-

vection $\mathcal{G}\Theta\rho_0 C_p$. The diabatic across-isotherm volume flux $\mathcal{G}\Theta\rho_0 C_p$ is itself a consequence of surface forcing and mixing. It is also dependent upon an arbitrary choice of reference temperature Θ_{ref}. *Palmer and Haines* [2009] and *Holmes et al.* [2019] sought to exclude the reference temperature-dependent diathermal advection term from the heat budget, *Palmer and Haines* [2009] by setting reference temperature as the mean temperature of the volume bounded by an isotherm, and *Holmes et al.* [2019] by combining the heat and volume budgets into a budget for *internal heat content* that is independent of the reference temperature. The internal heat content tendency in *Holmes et al.* [2019] is directly related to changes in surface fluxes and mixing,

$$\frac{\partial \mathcal{H}_I}{\partial t}(\Theta, t) = \rho_0 C_p \int_{\Theta}^{\infty} \frac{\partial \mathcal{V}}{\partial t}(\Theta, t) d\Theta = \mathcal{F}(\Theta, t) + \mathcal{M}(\Theta, t), \tag{4}$$

where $\mathcal{F}(\Theta, t)$ is the surface heat flux into the volume $\mathcal{V}(\Theta, t)$, including the component associated with surface volume fluxes (see *Holmes et al.* [2019]). $\mathcal{M}(\Theta, t)$ is the heat transport across the Θ isotherm due to mixing.

OHC change in the fixed-temperature framework results in changes in the volume distribution of temperature classes (i.e., $d\mathcal{V}/dt$ or equivalently dp/dt). OHC change in the temperature percentiles results in changes in the temperature of the isotherms that bound a given volume percentile of the ocean (i.e., $d\Theta^p/dt$). The heat content in the temperature percentiles in equation (3) may thus be related to the OHC in the fixed-temperature framework in equation (1) using the slope of the cumulative volume distribution of the ocean in fixed-temperature coordinates (figure 1):

$$\frac{\partial \Theta^p}{\partial t} = \frac{\partial p}{\partial t}\left(\frac{\partial \Theta^p}{\partial p}\right). \tag{5}$$

This transformation between fixed-temperature and temperature-percentile co-ordinates allows us to map between the internal heat content tendency in *Holmes et al.* [2019] and the equivalent heat content tendency in the tracer-percentile framework. Combining equations (4) and (5), we obtain the OHC tendency in temperature percentiles:

$$\frac{\partial \mathcal{H}}{\partial t}(p, t) = 0.01\mathcal{V}_T \rho_0 C_p \int_0^p \frac{\partial \Theta^p}{\partial t}(p, t) dp = \mathcal{F}(p, t) + \mathcal{M}(p, t). \tag{6}$$

Equation (6) shows that in temperature percentiles the total heat content tendency is, like the internal heat content tendency in the fixed-temperature framework [equation (4)], unaffected by the across-isotherm heat transport associated with across-isotherm volume transport, as this term is by definition zero. Rather, changes in the global heat content can be directly attributed to diabatic surface fluxes $\mathcal{F}(p, t)$ and mixing $\mathcal{M}(p, t)$.

3 Data

3.1 Observations

We use a hybrid observational dataset which combines observations of monthly-averaged, in-situ temperature from two optimally-interpolated gridded datasets:

1. A temperature field developed by *Cheng and Zhu* [2016] with temperature casts sourced from the *World Ocean Database*, hereafter referred to as the *Institute of Atmospheric Physics (IAP) dataset*, and
2. A temperature field from the UK Met Office Hadley Centre Enhanced Ocean Data Assimilation and Climate prediction (ENACT) version 4 (*EN4*, subversion EN.4.2.1,

with *Gouretski and Reseghetti* [2010] corrections, see *Good et al.* [2013] for more details).

The IAP dataset is formulated to reduce sampling errors which arise due to scarce observations prior to the introduction of the Argo program. This is accomplished by combining observed temperature casts with the error covariance matrix from an ensemble of CMIP5 models [*Cheng and Zhu*, 2016; *Cheng et al.*, 2017]. The IAP data is only available for the top 2000m of the ocean, so we fill the deep ocean with temperature data from EN4. Our hybrid dataset extends from January 1970 to December 2014, and has a $1^\circ \times 1^\circ$ horizontal grid with 53 vertical levels. We convert in-situ temperature in observations to conservative temperature as it is proportional to potential enthalpy [*McDougall*, 2003; *Graham and McDougall*, 2013]. Monthly-averaged variables are binned in temperature space and time-averaged to yield annual means. Tendency terms are subsequently calculated as the linear trend of a given volume percentile between 1970 and 2014. Marginal seas, namely, the Mediterranean, Red, Baltic, and Black Seas, and the Persian Gulf and Hudson Bay, are excluded from the analysis. Reference density is assumed to be $\rho_0 = 1035\ \mathrm{kgm}^{-3}$ and the specific heat $C_p = 4000\ \mathrm{Jkg}^{-1}\mathrm{K}^{-1}$.

Uncertainty in the observations is estimated by repeating the analysis 1000 times with temperatures perturbed in a random normal distribution based on standard error estimates from the IAP dataset. Note that the uncertainty obtained from this method is smaller than the standard error of the linear fit used to obtain tendencies. Standard error is not estimated below 1000m in EN4 [*Good et al.*, 2013]. Therefore, in this analysis, uncertainty is represented by the standard error of the linear regression of the relevant terms. Note that the auto-correlation coefficient of the OHC tendency is above 0.95 for a time lag of 1 year at all volume percentiles, so the standard error from the linear regression may be thought of as a measure of how subsampling different years which have largely independent data might affect our analysis.

3.2 Models

Temperature and surface fluxes in thirty climate models that form part of the Climate Model Intercomparison Project phase 6 [CMIP6; *Eyring et al.*, 2016] are analysed (see Table S1). We focus on the historical experiment, which branches from the pre-industrial control (piControl) experiment and covers the time period 1850–2014. The historical runs include all natural and anthropogenic forcing. The difference between conservative and potential temperature is negligible, so we use the more widely-reported potential temperature in the CMIP6 calculations. We use monthly-averaged data from the 1970–2014 period and mask the Mediterranean, Red, Baltic, and Black Seas, and the Persian Gulf and Hudson Bay prior to analysis. Model drift is removed in all variables of interest in order to avoid contamination of any forced trends and to ensure closure of the global ocean heat budget [*Irving et al.*, 2020, see supplementary information]. The models used in this study archive valid monthly timescale potential temperature data, *thetao*, grid cell volume, *volcello*, and surface flux data, *hfds* for both the historical and piControl experiments. As with the observations, the monthly-averaged surface fluxes, grid cell volume and temperature are binned into temperature co-ordinates and time-averaged to yield annual means. The surface flux tendency $\mathcal{F}(\Theta^*, t)$ is calculated as the time-derivative of the time-integrated annual mean surface flux difference between the historical and pre-industrial control experiments. More details of this procedure are provided in the supplementary information. The binned diagnostics are then interpolated from fixed-temperature coordinates to temperature percentiles. The slope of the linear regression of the binned variables *thetao* and *volcello* in temperature percentiles provides an estimate of $\partial\mathcal{H}/\partial t$ for the models. Details of the individual model members that make up the suite of CMIP6 models analysed are provided in the supplementary information. In the analysis of CMIP6 models, the reference density is $\rho_0 = 1035\ \mathrm{kgm}^{-3}$, and the specific heat is $C_p = 4000\ \mathrm{Jkg}^{-1}\mathrm{K}^{-1}$,

unless otherwise specified by modelling groups in the relevant documentation (see references in Table S1).

To complement our analysis of the standard CMIP6 diagnostics, we assesses a range of additional outputs from the ACCESS-CM2 historical and piControl simulations which are not archived as part of CMIP6 [*Bi et al.*, 2020]. The standard surface heat flux diagnostic reported for CMIP6 (*hfds*) does not account for the redistribution of shortwave radiation into the ocean interior (which is absorbed at a temperature different to the SST). To evaluate the impact of this missing process on our results, as well as the role of specific mixing processes, we use precise ocean heat budget tendency diagnostics from the ACCESS-CM2 simulations. These tendency diagnostics are binned into fixed-temperature coordinates using the monthly-averaged temperature distribution.

4 Results

We quantify the integrated heat content tendency $\partial\mathcal{H}(p,t)/\partial t$ in the observations and CMIP6 models, the integrated surface flux tendency $\mathcal{F}$ in the CMIP6 models, and the inferred mixing tendency $\mathcal{M}$ in figure 2. The mixing in figure 2c is the residual between figures 2a and 2b (with the exception of the ACCESS-CM2 diagnostic term in purple), and includes any errors associated with binning, the neglect of shortwave penetration and time-averaging. By construction, the integrated curves in figure 2a, b and c are 0 at $p = 0\%$.

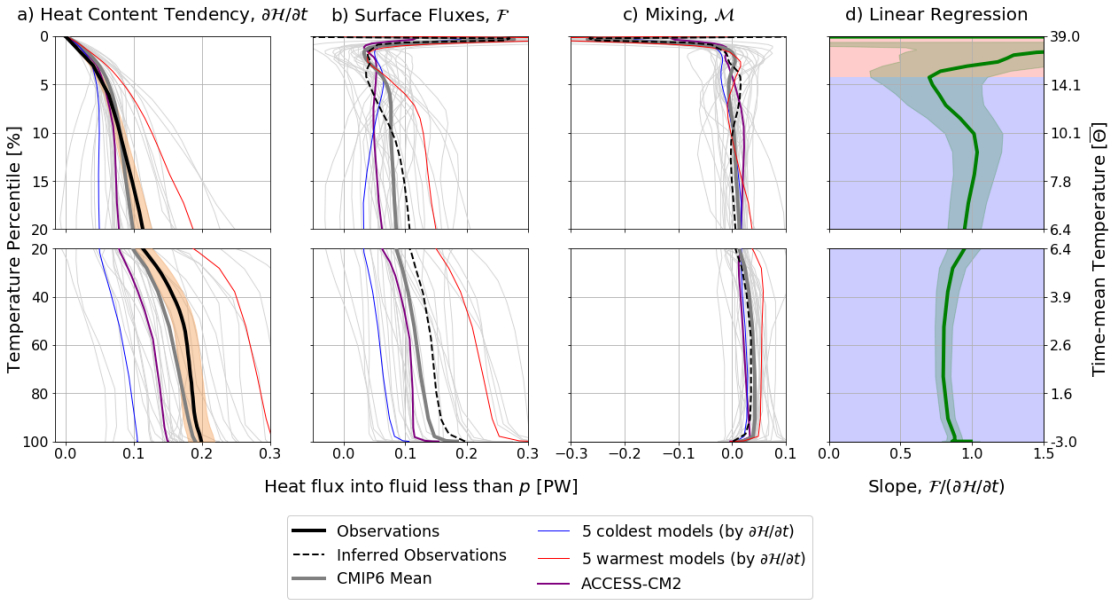

Figure 2. The a) heat content tendency $\partial\mathcal{H}(p,t)/\partial t$, b) surface heat flux trends $\mathcal{F}$, and c) inferred mixing changes $\mathcal{M}$ integrated from hot to cold (i.e., values at $p = 100\%$ are the global integral). Tendencies in a) and b) are calculated as the linear trend in heat content or surface flux at constant temperature-percentile from 1970 to 2014. Orange shading shows the standard error (2σ) of the linear trend in heat content. d) Linear regression of the integrated $\mathcal{F}$ and $\partial\mathcal{H}/\partial t$ at each temperature-percentile in the CMIP6 models. Green line indicates the slope of the linear regression and green shading shows the standard error of the linear fit. The red and blue shading represents the sub-tropical and sub-polar oceans, respectively, based on the time-mean surface temperature bounds $28°C > \overline{\Theta} > 15°C$ and $\overline{\Theta} < 15°C$, respectively, from *Grist et al.* [2016]. The tropics (defined as $\overline{\Theta} > 28°C$) are not visible in this plot. The warmest 20% volume is expanded in these plots. A secondary y-axis marks the time-mean temperature $\overline{\Theta}$ corresponding to each temperature-percentile.

The heat content increases across all temperature percentiles in the observations and the majority of CMIP6 models (figure 2a). There is a reasonable match in OHC tendency between the CMIP6 mean and the observations (compare black and gray lines in figure 2a), though there is a substantial spread between the models in the CMIP6 ensemble (compare the blue and red lines in figure 2a), and the ensemble-mean OHC is less than the observed OHC for $p > 10\%$. Surface flux tendencies again show a large spread between models (figure 2b).

The strong increase in surface fluxes in the warmest $\sim 2.5\%$ of the ocean is largely balanced by mixing, which fluxes this additional heat toward cooler temperature classes. This region corresponds to warm temperatures ($\Theta >\sim 25°C$), which collapse to a narrow temperature-percentile range at the top of the figure. There is also an anomalous divergence of heat due to mixing (driving a cooling tendency from mixing) out of the coldest 40% of waters and an anomalous convergence of heat due to mixing (driving a warming tendency from mixing) between $10\% < p < 60\%$. The largest cooling tendency from mixing occurs out of the 5% coldest waters.

The surface flux tendencies in figure 2b do not account for shortwave redistribution. In addition, mixing is not a defined CMIP6 variable, and is not available for many CMIP6 models. Therefore, it remains unclear how much of the the difference between heat content tendency and surface forcing shown in figure 2c is due to mixing, and how much is due to shortwave redistribution and other errors. To explore this, we analyse the ocean model component of a single CMIP6 model member - ACCESS-CM2 - applying the diagnostic framework of *Holmes et al.* [2019] to explicitly calculate mixing and the effect of shortwave redistribution. The breakdown of processes in ACCESS-CM2 (purple lines in figure 2) largely aligns with the inferred diabatic fluxes in the rest of the CMIP6 models. There is a cooling tendency from mixing between $60\% < p < 100\%$ and a warming tendency from mixing between $10\% < p < 60\%$. In addition, the strong increase in surface fluxes at $0\% < p < 2.5\%$ is reduced by 17.7% when shortwave redistribution is taken into account (not shown). The mixing in these volume classes consequently does not change as much as inferred from the CMIP6 models.

It is not possible to calculate surface flux tendencies and mixing from coarse resolution observational datasets. Instead, reanalysis products are often used which rely on ocean models (e.g., *Liang and Yu* [2016]). The tracer-percentile framework allows us to infer bulk surface flux and mixing quantities directly from observed OHC tendencies using the CMIP6 relationships in figure 2. A linear regression analysis is performed between integrated surface flux tendencies and heat content tendencies at each temperature-percentile for each of the CMIP6 models, with the slope and error of the regression shown in figure 2d. The inferred observed surface flux may be calculated using this slope as $\mathcal{F} = \partial\mathcal{H}/\partial t \times Slope$. There is significant error in the linear regression in the tropical and sub-tropical regions (below $p \approx 10\%$). However, at temperature percentiles colder than $p \approx 10\%$ (i.e. the coldest 90% of the ocean), there is a statistically significant correlation between heat content and surface flux tendencies. Between $10\% < p < 20\%$, the slope of the correlation is close to 1, implying that excess heat entering the surface at these volume classes tends to remain there. By construction, the slope should be 1 at $p = 100\%$, as there is no mixing in a globally integrated sense. Any deviation from 1 is due to diagnosed non-closure of the ocean heat budget in the models [*Irving et al.*, 2020]. Assuming the relationship between surface fluxes and OHC tendency in the CMIP6 models holds for the real ocean, we infer the integrated surface flux-driven tendency and mixing-driven tendency as a function of temperature percentiles for the observations (dashed lines in figures 2b and c). Note that the inferred surface flux and mixing profile is only statistically significant above a temperature-percentile of $\sim 10\%$. A further breakdown of the observed OHC tendency and its inferred surface fluxes and mixing is discussed in section 5.

The OHC tendency in the CMIP6 mean is less than that in the observations (Figure 2a). The tracer-percentile framework allows us to identify volume classes (organ-

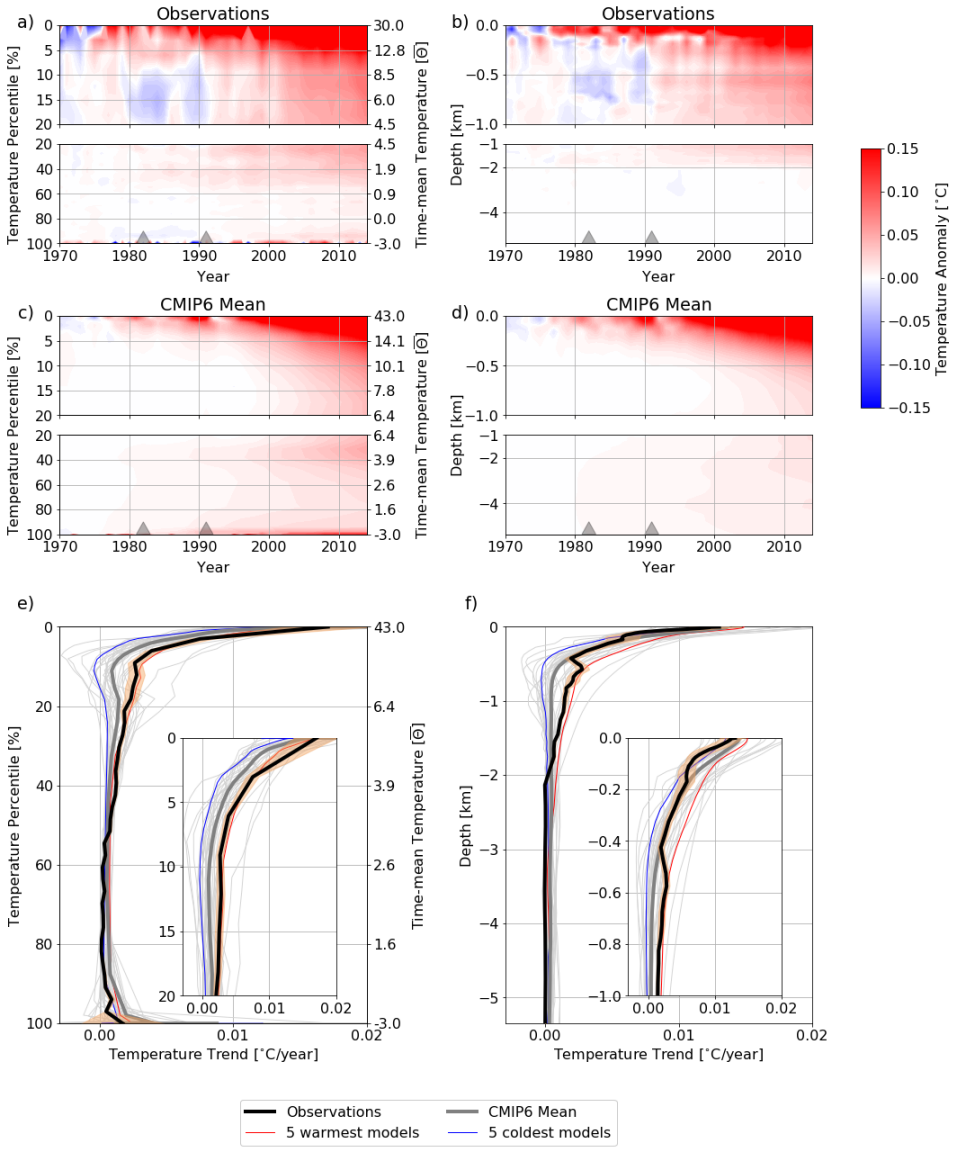

Figure 3. Global temperature anomaly calculated relative to a 1970-1980 baseline in a) temperature percentiles, and b) fixed depth in the observations. c) and d) same as above but for the CMIP6 ensemble-mean. Grey triangles indicate volcanic eruptions of El Chichón (1982) and Pinatubo (1991). e) and f) Temperature anomaly trends (°C/year) calculated from the linear trend in temperature at constant temperature-percentile and depth, respectively. Orange shading shows the standard error (2σ) of the linear trend in temperature anomaly. The warmest 20% of the ocean (or the top 1000 metres in panels b and d) use an expanded y-axis. A secondary axis marks the time-mean temperature $\overline{\Theta}$ corresponding to the temperature-percentile in a), c) and e).

ised by temperature) where the cold anomaly that leads to this bias is introduced, and whether it can be traced back to mixing or surface flux changes. To this end, we plot the temperature anomaly in temperature percentiles and fixed depths in the observations and CMIP6 models in figure 3. Recall from section 2 that the temperature anomaly in temperature percentiles is proportional to the percentile derivative of the OHC tendency, i.e., $\frac{\partial \Theta^p}{\partial t} = \frac{100}{\mathcal{V}_T \rho_0 C_p} \frac{\partial}{\partial p} \left(\frac{\partial \mathcal{H}}{\partial t} \right)$.

In tracer-percentiles temperature anomalies are qualitatively similar to the fixed-depth framework (figures 3a-d). Note in particular the similarity of the observed negative temperature anomaly between 1980 and 1990 in tracer-percentiles and fixed-depth coordinates (compare figures 3a and 3b), as well as the persistent cooler (compared to observations) signal in the CMIP6 mean between $5\% < p < 20\%$ and $-1\,\text{km} < z < -0.25\,\text{km}$ (compare figures 3c and 3d, and thick grey lines in 3e and 3f). A key difference between the temperature percentiles and fixed depth is the warm anomaly in the coldest 20% temperature percentiles, which cannot be seen in the deep ocean ($z < -4\,\text{km}$). The coldest percentiles include surface polar waters. Therefore, where warming of surface polar waters is conflated with changes in the surface sub-tropics and tropics at fixed depth, surface polar warming is emphasised at the coldest temperature percentiles. Analysis of temperature anomalies of water colder than 0° at fixed-depth (not shown) confirms that the majority of the warming in the coldest percentiles originates at the surface of the ocean. The temperature trend over the full time period, shown in temperature-percentile and fixed-depth coordinates in figures 3e and 3f respectively, reveals that the observed annual temperature anomaly has a number of 'kinks' in the sub-surface ($z \approx [0.2, 0.5]$ km) in fixed-depth coordinates which are not visible in the tracer-percentile framework. We posit these kinks may be associated with XBT corrections in the observations [*Abraham et al.*, 2013] or internal variability.

The CMIP6 models exhibit a weaker warming trend in the $\sim$ 40% warmest volume classes in the ocean, particularly between $5\% < p < 20\%$ (compare black and gray lines in figure 3e). Revisiting the CMIP6 linear regression in figure 2d, we conclude that the weaker modelled warming trend in volume classes above $\sim$ 10% is likely attributed to biases in surface flux changes (as the regression coefficient is close to 1 at these percentiles). These surface flux trends may be inaccurate in magnitude or spatial pattern, leading to heat entering the ocean at incorrect volume classes. Past research with CMIP5 models has also identified a consistent sea surface temperature (SST) bias in climate models - particularly a warm bias in the Southern Ocean SSTs [*Sallée et al.*, 2013; *Meijers*, 2014]. There is evidence this SST bias still exists in the current generation of CMIP6 models [*Beadling et al.*, 2020]. In fact, SSTs and surface fluxes are tightly coupled, so the true reason for the CMIP6 bias is likely to be a combination of inaccuracies in both [*Hyder et al.*, 2018]. A possible explanation for the weaker CMIP6 warming trend may also be that the CMIP6 models have biased mixing, which would imply a surface flux bias elsewhere.

5 Discussion and Conclusions

We introduce a novel diagnostic framework (termed the *tracer-percentile framework*) which we apply to ocean temperature and use to directly relate changes in OHC to changes in diabatic heat fluxes, namely, surface forcing and mixing. By quantifying the heat content in and transport across temperature percentiles (ordered from warmest to coldest), we exclude adiabatic processes and avoid regime changes associated with shifting isotherms in a warming ocean. We are thus able to trace changes in OHC to changes in surface fluxes and mixing using a combination of traditional observational hydrographic datasets and CMIP6 models. Comparing heat content tendency and surface fluxes in a suite of thirty CMIP6 models from 1970 to 2014, we establish that changes in the coldest 90% of the ocean may be traced to changes in the net surface heat flux into volume classes in the sub-polar ocean. Assuming that the linear regression between OHC tendency and surface flux changes in the CMIP6 climate models holds for the real ocean, we infer changes in sub-polar surface heat fluxes and mixing based on observed OHC trends.

Figure 4 summarises the observed OHC tendency and the inferred surface flux and mixing tendencies in temperature-percentile layers in the ocean. We find that $\sim$ 60% of the anomalous surface flux into the ocean (sum of all arrows in figure 4 save the red arrow) enters 23% of the surface ocean (sum of all outcrop lengths in figure 4 except the

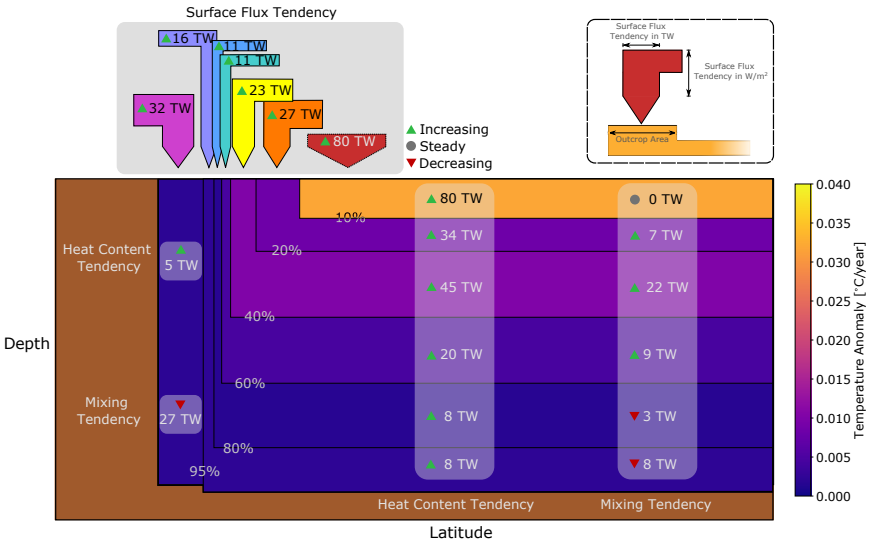

Figure 4. Observed temperature anomalies, heat content tendencies, and inferred surface flux and mixing tendencies using the tracer-percentile framework. The OHC tendency, surface fluxes and mixing are calculated as the derivative of the solid and dashed black curves in figures 2 a, b and c. Note that while the Southern Hemisphere is schematised here, the values shown are for the global ocean. By construction, mixing tendencies sum to zero globally, and a decrease in down-gradient mixing implies a reduction in OHC tendency in that layer, and vice versa. The area of each layer in the schematic is proportional to its volume, and the outcrop length at the top surface is proportional to the outcrop area of the layer. The width of the surface flux arrows is proportional to their value (in TW), and the height is proportional to the surface flux per unit area (in W/m^2). Surface flux and mixing trends in the 10% warmest ocean volume are uncertain due to the poor linear fit in CMIP6 models.

outcrop of the warmest 10% volume), which represents the outcrop area of the temperature-percentile bounding 90% of the ocean by volume. Therefore, minor changes to SSTs or surface fluxes overlying this relatively small surface area of the ocean may have profound impacts on the mean stratification and ocean circulation. Down-gradient mixing is decreasing across the 40%-95% percentiles, and increasing across the 10% and 20% percentiles according to our analysis. The strongest decrease in mixing occurs across the 95% percentile.

For the first time, the tracer-percentile framework allows us to link observed OHC changes to surface flux tendencies and the surface area over which they enter. This result enables the identification of the cause of biases in OHC tendencies in climate models. We identify a cooling bias in CMIP6 models which is apparent at both fixed depth and temperature percentiles. We trace this cooling bias to anomalous changes in surface forcing into the same temperature percentiles. The surface flux field may have either incorrect magnitude or incorrect spatial distribution, the SSTs which define the volume classes into which the surface fluxes enter may be biased in many ocean models, or the mixing in all CMIP6 models may be biased (with a surface flux bias elsewhere).

The insights from the tracer-percentile framework motivate a mechanistic approach to future explorations of OHC tendency and its diabatic contributors. The global analysis presented here indicates that surface fluxes over a small region of the ocean contribute to OHC changes in the vast majority of the ocean volume. Therefore, understanding the mechanisms which lead to increases in surface fluxes in these regions (and indeed to surface flux biases in models) is crucial. Mixing also displays variability between volume classes, and understanding the processes which drive these changes in mixing is vital to gaining a complete picture of historical and future changes in OHC. The tracer-percentile framework is a versatile tool, and future efforts will work towards expanding the use-cases of the tracer-percentile framework and further understanding oceanic and atmospheric dynamics in the context of temperature and other tracers.

Acknowledgments

We acknowledge the World Climate Research Programme, which, through its Working Group on Coupled Modelling, coordinated and promoted CMIP6. We thank the climate modeling groups for producing and making available their model output, the Earth System Grid Federation (ESGF) for archiving the data and providing access, and the multiple funding agencies who support CMIP6 and ESGF. All data used is publicly available, CMIP6 data from the ESGF (esgf-node.llnl.gov/search/cmip6), EN4 data from the Met Office Hadley Centre (https://www.metoffice.gov.uk/hadobs/en4/download.html) and IAP data from the Chinese Academy of Sciences (https://climatedataguide.ucar.edu/climate-data/ocean-temperature-analysis-and-heat-content-estimate-institute-atmospheric-physics). Modeling and analysis were undertaken using facilities at the National Computational Infrastructure (NCI), which is supported by the Australian Government. This work is supported by the Australian Research Council (ARC) Centre of Excellence for Climate Extremes, the Centre for Southern Hemisphere Oceans Research (a joint research centre between the QNLM and the CSIRO) and the ARC Discovery Project funding scheme (DP190101173).

References

Abraham, J. P., M. Baringer, N. L. Bindoff, T. Boyer, L. J. Cheng, J. A. Church, J. L. Conroy, C. M. Domingues, J. T. Fasullo, J. Gilson, G. Goni, S. A. Good, J. M. Gorman, V. Gouretski, M. Ishii, G. C. Johnson, S. Kizu, J. M. Lyman, A. M. Macdonald, W. J. Minkowycz, S. E. Moffitt, M. D. Palmer, A. R. Piola, F. Reseghetti, K. Schuckmann, K. E. Trenberth, I. Velicogna, and J. K. Willis (2013), A review of global ocean tem-

perature observations: Implications for ocean heat content estimates and climate change, *Reviews of Geophysics*, *51*(3), 450–483, doi:10.1002/rog.20022.

Beadling, R. L., J. L. Russell, R. J. Stouffer, M. Mazloff, L. D. Talley, P. J. Goodman, J. B. Sallée, H. T. Hewitt, P. Hyder, and A. Pandde (2020), Representation of Southern Ocean properties across Coupled Model Intercomparison Project generations: CMIP3 to CMIP6 Representation of Southern Ocean properties across Coupled Model Intercomparison Project generations: CMIP3 to CMIP6, *Journal of Climate*, *33*(15), 6555–6581, doi:10.1175/jcli-d-19-0970.1.

Bi, D., M. Dix, S. Marsland, S. O'Farrell, A. Sullivan, R. Bodman, R. Law, I. Harman, J. Srbinovsky, H. A. Rashid, P. Dobrohotoff, C. Mackallah, H. Yan, A. Hirst, A. Savita, F. B. Dias, M. Woodhouse, R. Fiedler, and A. Heerdegen (2020), Configuration and spin-up of ACCESS-CM2, the new generation Australian Community Climate and Earth System Simulator Coupled Model, *Journal of Southern Hemisphere Earth Systems Science*, doi:10.1071/es19040.

Cheng, L., and J. Zhu (2016), Benefits of CMIP5 multimodel ensemble in reconstructing historical ocean subsurface temperature variations, *Journal of Climate*, *29*(15), 5393–5416, doi:10.1175/jcli-d-15-0730.1.

Cheng, L., K. E. Trenberth, J. Fasullo, T. Boyer, J. Abraham, and J. Zhu (2017), Improved estimates of ocean heat content from 1960 to 2015, *Science Advances*, *3*(3), e1601,545, doi:10.1126/sciadv.1601545.

Church, J. A., and N. J. White (2011), Sea-Level Rise from the Late 19th to the Early 21st Century, *Surveys in Geophysics*, *32*(4-5), 585–602, doi:10.1007/s10712-011-9119-1.

Cummins, P. F., D. Masson, and O. A. Saenko (2016), Vertical heat flux in the ocean: Estimates from observations and from a coupled general circulation model, *Journal of Geophysical Research: Oceans*, *121*(6), 3790–3802, doi:10.1002/2016jc011647.

Domingues, C. M., J. A. Church, N. J. White, P. J. Gleckler, S. E. Wijffels, P. M. Barker, and J. R. Dunn (2008), Improved estimates of upper-ocean warming and multi-decadal sea-level rise., *Nature*, *453*(7198), 1090–3, doi:10.1038/nature07080.

Evans, D. G., J. Toole, G. Forget, J. D. Zika, A. C. N. Garabato, A. J. G. Nurser, and L. Yu (2017), Recent Wind-Driven Variability in Atlantic Water Mass Distribution and Meridional Overturning Circulation, *Journal of Physical Oceanography*, *47*(3), doi:10.1175/JPO-D-16-0089.1.

Eyring, V., S. Bony, G. A. Meehl, C. A. Senior, B. Stevens, R. J. Stouffer, and K. E. Taylor (2016), Overview of the Coupled Model Intercomparison Project Phase 6 (CMIP6) experimental design and organization, *Geoscientific Model Development*, *9*(5), 1937–1958, doi:10.5194/gmd-9-1937-2016.

Gnanadesikan, A., R. D. Slater, P. S. Swathi, and G. K. Vallis (2005), The Energetics of Ocean Heat Transport, *Journal of Climate*, *18*(14), 2604–2616, doi:10.1175/jcli3436.1.

Good, S. A., M. J. Martin, and N. A. Rayner (2013), EN4: Quality controlled ocean temperature and salinity profiles and monthly objective analyses with uncertainty estimates, *Journal of Geophysical Research: Oceans*, *118*(12), 6704–6716, doi:10.1002/2013jc009067.

Gouretski, V., and F. Reseghetti (2010), On depth and temperature biases in bathythermograph data: Development of a new correction scheme based on analysis of a global ocean database, *Deep Sea Research Part I: Oceanographic Research Papers*, *57*(6), 812–833, doi:10.1016/j.dsr.2010.03.011.

Graham, F. S., and T. J. McDougall (2013), Quantifying the Nonconservative Production of Conservative Temperature, Potential Temperature, and Entropy, *Journal of Physical Oceanography*, *43*(5), 838–862, doi:10.1175/jpo-d-11-0188.1.

Gregory, J., D. Bi, M. Collier, M. Dix, A. Hirst, A. Hu, M. Huber, R. Knutti, S. Marsland, M. Meinshausen, H. Rashid, L. Rotstayn, A. Schurer, and J. Church (2013), Climate models without preindustrial volcanic forcing underestimate historical ocean thermal expansion, *Geophysical Research Letters*, *40*(8), 1600–1604, doi:10.1002/grl.50339.

Gregory, J. M. (2000), Vertical heat transports in the ocean and their effect on time-dependent climate change, *Climate Dynamics*, *16*(7), 501–515, doi: 10.1007/s003820000059.

Grist, J. P., S. A. Josey, J. D. Zika, D. G. Evans, and N. Skliris (2016), Assessing recent air-sea freshwater flux changes using a surface temperature-salinity space framework, *Journal of Geophysical Research: Oceans*, *121*(12), 8787–8806, doi: 10.1002/2016jc012091, grist et al., 2016: Great paper to be cited in future.

Groeskamp, S., S. M. Griffies, D. Iudicone, R. Marsh, A. J. G. Nurser, and J. D. Zika (2019), The Water Mass Transformation Framework for Ocean Physics and Biogeochemistry, *Annual Review of Marine Science*, *11*(1), 271–305, doi:10.1146/annurev-marine-010318-095421.

Holmes, R. M., J. D. Zika, and M. H. England (2019), Diathermal Heat Transport in a Global Ocean Model, *Journal of Physical Oceanography*, *49*(1), 141–161, doi: 10.1175/jpo-d-18-0098.1.

Hyder, P., J. M. Edwards, R. P. Allan, H. T. Hewitt, T. J. Bracegirdle, J. M. Gregory, R. A. Wood, A. J. S. Meijers, J. Mulcahy, P. Field, K. Furtado, A. Bodas-Salcedo, K. D. Williams, D. Copsey, S. A. Josey, C. Liu, C. D. Roberts, C. Sanchez, J. Ridley, L. Thorpe, S. C. Hardiman, M. Mayer, D. I. Berry, and S. E. Belcher (2018), Critical Southern Ocean climate model biases traced to atmospheric model cloud errors, *Nature Communications*, *9*(1), 3625, doi:10.1038/s41467-018-05634-2.

Irving, D., W. Hobbs, J. Church, and J. Zika (2020), A Mass and Energy Conservation Analysis of Drift in the CMIP6 Ensemble, *Journal of Climate*, pp. 1–43, doi: 10.1175/jcli-d-20-0281.1.

Kuhlbrodt, T., J. M. Gregory, and L. C. Shaffrey (2015), A process-based analysis of ocean heat uptake in an AOGCM with an eddy-permitting ocean component, *Climate Dynamics*, *45*(11-12), 3205–3226, doi:10.1007/s00382-015-2534-0.

Liang, X., and L. Yu (2016), Variations of the Global Net Air–Sea Heat Flux during the "Hiatus" Period (2001–10), *Journal of Climate*, *29*(10), 3647–3660, doi:10.1175/jcli-d-15-0626.1.

Liang, X., C. Wunsch, P. Heimbach, and G. Forget (2015), Vertical Redistribution of Oceanic Heat Content, *Journal of Climate*, *28*(9), 3821–3833, doi:10.1175/jcli-d-14-00550.1.

Liang, X., C. G. Piecuch, R. M. Ponte, G. Forget, C. Wunsch, and P. Heimbach (2017), Change of the Global Ocean Vertical Heat Transport over 1993–2010, *Journal of Climate*, *30*(14), 5319–5327, doi:10.1175/jcli-d-16-0569.1.

Lin, I.-I., G. J. Goni, J. A. Knaff, C. Forbes, and M. M. Ali (2013), Ocean heat content for tropical cyclone intensity forecasting and its impact on storm surge, *Natural Hazards*, *66*(3), 1481–1500, doi:10.1007/s11069-012-0214-5.

McDougall, T. J. (2003), Potential Enthalpy: A Conservative Oceanic Variable for Evaluating Heat Content and Heat Fluxes, *Journal of Physical Oceanography*, *33*(5), 945–963, doi:10.1175/1520-0485(2003)033<0945:peacov>2.0.co;2.

Meijers, A. J. S. (2014), The Southern Ocean in the Coupled Model Intercomparison Project phase5, *Philosophical Transactions of the Royal Society A: Mathematical, Physical and Engineering Sciences*, *372*(2019), 20130,296, doi:10.1098/rsta.2013.0296.

Morrison, A. K., O. A. Saenko, A. M. Hogg, and P. Spence (2013), The role of vertical eddy flux in Southern Ocean heat uptake, *Geophysical Research Letters*, *40*(20), 5445–5450, doi:10.1002/2013gl057706.

Palmer, M. D., and K. Haines (2009), Estimating Oceanic Heat Content Change Using Isotherms, *Journal of Climate*, *22*(19), 4953–4969, doi:10.1175/2009jcli2823.1.

Sallée, J., E. Shuckburgh, N. Bruneau, A. J. S. Meijers, T. J. Bracegirdle, Z. Wang, and T. Roy (2013), Assessment of Southern Ocean water mass circulation and characteristics in CMIP5 models: Historical bias and forcing response, *Journal of Geophysical Research: Oceans*, *118*(4), 1830–1844, doi:10.1002/jgrc.20135.

Schuckmann, K. v., L. Cheng, M. D. Palmer, J. Hansen, C. Tassone, V. Aich, S. Adusumilli, H. Beltrami, T. Boyer, F. J. Cuesta-Valero, D. Desbruyères, C. Domingues, A. García-García, P. Gentine, J. Gilson, M. Gorfer, L. Haimberger, M. Ishii, G. C. Johnson, R. Killick, B. A. King, G. Kirchengast, N. Kolodziejczyk, J. Lyman, B. Marzeion, M. Mayer, M. Monier, D. P. Monselesan, S. Purkey, D. Roemmich, A. Schweiger, S. I. Seneviratne, A. Shepherd, D. A. Slater, A. K. Steiner, F. Straneo, M.-L. Timmermans, and S. E. Wijffels (2020), Heat stored in the Earth system: where does the energy go?, *Earth System Science Data*, *12*(3), 2013–2041, doi: 10.5194/essd-12-2013-2020.

Walin, G. (1982), On the relation between sea-surface heat flow and thermal circulation in the ocean, *Tellus*, *34*(2), 187–195, doi:10.3402/tellusa.v34i2.10801.

Watanabe, M., Y. Kamae, M. Yoshimori, A. Oka, M. Sato, M. Ishii, T. Mochizuki, and M. Kimoto (2013), Strengthening of ocean heat uptake efficiency associated with the recent climate hiatus, *Geophysical Research Letters*, *40*(12), 3175–3179, doi: 10.1002/grl.50541.

Wolfe, C. L., P. Cessi, J. L. McClean, and M. E. Maltrud (2008), Vertical heat transport in eddying ocean models, *Geophysical Research Letters*, *35*(23), doi: 10.1029/2008gl036138.

Zika, J. D., W. P. Sijp, and M. H. England (2013), Vertical Heat Transport by Ocean Circulation and the Role of Mechanical and Haline Forcing, *Journal of Physical Oceanography*, *43*(10), 2095–2112, doi:10.1175/jpo-d-12-0179.1.

Zika, J. D., N. Skliris, A. J. G. Nurser, S. A. Josey, L. Mudryk, F. Laliberté, and R. Marsh (2015), Maintenance and Broadening of the Ocean's Salinity Distribution by the Water Cycle, *Journal of Climate*, *28*(24), 9550–9560, doi:10.1175/jcli-d-15-0273.1.

References From the Supporting Information

Bentsen, M., D. J. L. Oliviè, y. Seland, T. Toniazzo, A. Gjermundsen, L. S. Graff, J. B. Debernard, A. K. Gupta, Y. He, A. Kirkev, J. Schwinger, J. Tjiputra, K. S. Aas, I. Bethke, Y. Fan, J. Griesfeller, A. Grini, C. Guo, M. Ilicak, I. H. H. Karset, O. A. Landgren, J. Liakka, K. O. Moseid, A. Nummelin, C. Spensberger, H. Tang, Z. Zhang, C. Heinze, T. Iversen, and M. Schulz (2019a), NCC NorESM2-MM model output prepared for CMIP6 CMIP historical, version 20191108.

Bentsen, M., D. J. L. Oliviè, y. Seland, T. Toniazzo, A. Gjermundsen, L. S. Graff, J. B. Debernard, A. K. Gupta, Y. He, A. Kirkev, J. Schwinger, J. Tjiputra, K. S. Aas, I. Bethke, Y. Fan, J. Griesfeller, A. Grini, C. Guo, M. Ilicak, I. H. H. Karset, O. A. Landgren, J. Liakka, K. O. Moseid, A. Nummelin, C. Spensberger, H. Tang, Z. Zhang, C. Heinze, T. Iversen, and M. Schulz (2019b), NCC NorESM2-MM model output prepared for CMIP6 CMIP piControl, version 20191108.

Bethke, I., Y. Wang, F. Counillon, M. Kimmritz, F. Fransner, A. Samuelsen, H. R. Langehaug, P.-G. Chiu, M. Bentsen, C. Guo, J. Tjiputra, A. Kirkev, D. J. L. Olivi\'e, y. Seland, Y. Fan, P. Lawrence, T. Eldevik, and N. Keenlyside (2019a), NCC NorCPM1 model output prepared for CMIP6 CMIP historical, version 20190914.

Bethke, I., Y. Wang, F. Counillon, M. Kimmritz, F. Fransner, A. Samuelsen, H. R. Langehaug, P.-G. Chiu, M. Bentsen, C. Guo, J. Tjiputra, A. Kirkev, D. J. L. Olivi\'e, y. Seland, Y. Fan, P. Lawrence, T. Eldevik, and N. Keenlyside (2019b), NCC NorCPM1 model output prepared for CMIP6 CMIP piControl, version 20190914.

Boucher, O., S. Denvil, A. Caubel, and M. A. Foujols (2018a), IPSL IPSL-CM6A-LR model output prepared for CMIP6 CMIP historical, version 20180803.

Boucher, O., S. Denvil, A. Caubel, and M. A. Foujols (2018b), IPSL IPSL-CM6A-LR model output prepared for CMIP6 CMIP piControl, version 20190522.

Danabasoglu, G. (2019a), NCAR CESM2 model output prepared for CMIP6 CMIP historical, version 20190308.

Danabasoglu, G. (2019b), NCAR CESM2-FV2 model output prepared for CMIP6 CMIP historical, version 20191120.

Danabasoglu, G. (2019c), NCAR CESM2-FV2 model output prepared for CMIP6 CMIP piControl, version 20191120.

Danabasoglu, G. (2019d), NCAR CESM2-WACCM-FV2 model output prepared for CMIP6 CMIP historical, version 20191120.

Danabasoglu, G. (2019e), NCAR CESM2-WACCM-FV2 model output prepared for CMIP6 CMIP piControl, version 20191120.

Danabasoglu, G. (2019f), NCAR CESM2-WACCM model output prepared for CMIP6 CMIP historical, version 20190808.

Danabasoglu, G. (2019g), NCAR CESM2-WACCM model output prepared for CMIP6 CMIP piControl, version 20190320.

Danabasoglu, G., D. Lawrence, K. Lindsay, W. Lipscomb, and G. Strand (2019), NCAR CESM2 model output prepared for CMIP6 CMIP piControl, version 20190320.

Dix, M., D. Bi, P. Dobrohotoff, R. Fiedler, I. Harman, R. Law, C. Mackallah, S. Marsland, S. O'Farrell, H. Rashid, J. Srbinovsky, A. Sullivan, C. Trenham, P. Vohralik, I. Watterson, G. Williams, M. Woodhouse, R. Bodman, F. B. Dias, C. Domingues, N. Hannah, A. Heerdegen, A. Savita, S. Wales, C. Allen, K. Druken, B. Evans, C. Richards, S. M. Ridzwan, D. Roberts, J. Smillie, K. Snow, M. Ward, and R. Yang (2019a), CSIRO-ARCCSS ACCESS-CM2 model output prepared for CMIP6 CMIP historical, version 20191108.

Dix, M., D. Bi, P. Dobrohotoff, R. Fiedler, I. Harman, R. Law, C. Mackallah, S. Marsland, S. O'Farrell, H. Rashid, J. Srbinovsky, A. Sullivan, C. Trenham, P. Vohralik, I. Watterson, G. Williams, M. Woodhouse, R. Bodman, F. B. Dias, C. Domingues, N. Hannah, A. Heerdegen, A. Savita, S. Wales, C. Allen, K. Druken, B. Evans, C. Richards, S. M. Ridzwan, D. Roberts, J. Smillie, K. Snow, M. Ward, and R. Yang (2019b), CSIRO-ARCCSS ACCESS-CM2 model output prepared for CMIP6 CMIP piControl, version 20191112.

EC-Earth (2019a), EC-Earth-Consortium EC-Earth3 model output prepared for CMIP6 CMIP historical, version 20200310.

EC-Earth (2019b), EC-Earth-Consortium EC-Earth3 model output prepared for CMIP6 CMIP piControl, version 20200312.

EC-Earth (2019c), EC-Earth-Consortium EC-Earth3-Veg model output prepared for CMIP6 CMIP historical, version 20200225.

EC-Earth (2019d), EC-Earth-Consortium EC-Earth3-Veg model output prepared for CMIP6 CMIP piControl, version 20200226.

EC-Earth (2020a), EC-Earth-Consortium EC-Earth3-Veg-LR model output prepared for CMIP6 CMIP historical, doi:10.22033/esgf/cmip6.4707.

EC-Earth (2020b), EC-Earth-Consortium EC-Earth3-Veg-LR model output prepared for CMIP6 CMIP piControl, doi:10.22033/esgf/cmip6.4849.

Huang, W. (2019a), THU CIESM model output prepared for CMIP6 CMIP historical, doi: 10.22033/esgf/cmip6.8843.

Huang, W. (2019b), THU CIESM model output prepared for CMIP6 CMIP piControl, doi: 10.22033/esgf/cmip6.8849.

Jungclaus, J., M. Bittner, K.-H. Wieners, F. Wachsmann, M. Schupfner, S. Legutke, M. Giorgetta, C. Reick, V. Gayler, H. Haak, P. d. Vrese, T. Raddatz, M. Esch, T. Mauritsen, J.-S. v. Storch, J. Behrens, V. Brovkin, M. Claussen, T. Crueger, I. Fast, S. Fiedler, S. Hagemann, C. Hohenegger, T. Jahns, S. Kloster, S. Kinne, G. Lasslop, L. Kornblueh, J. Marotzke, D. Matei, K. Meraner, U. Mikolajewicz, K. Modali, W. Müller, J. Nabel, D. Notz, K. Peters, R. Pincus, H. Pohlmann, J. Pongratz, S. Rast, H. Schmidt, R. Schnur, U. Schulzweida, K. Six, B. Stevens, A. Voigt, and E. Roeckner (2019a), MPI-M MPI-ESM1.2-HR model output prepared for CMIP6 CMIP historical, version 20190710.

Jungclaus, J., M. Bittner, K.-H. Wieners, F. Wachsmann, M. Schupfner, S. Legutke, M. Giorgetta, C. Reick, V. Gayler, H. Haak, P. d. Vrese, T. Raddatz, M. Esch, T. Mauritsen, J.-S. v. Storch, J. Behrens, V. Brovkin, M. Claussen, T. Crueger, I. Fast, S. Fiedler, S. Hagemann, C. Hohenegger, T. Jahns, S. Kloster, S. Kinne, G. Lasslop, L. Kornblueh, J. Marotzke, D. Matei, K. Meraner, U. Mikolajewicz, K. Modali, W. Müller, J. Nabel, D. Notz, K. Peters, R. Pincus, H. Pohlmann, J. Pongratz, S. Rast, H. Schmidt, R. Schnur, U. Schulzweida, K. Six, B. Stevens, A. Voigt, and E. Roeckner (2019b), MPI-M MPI-ESM1.2-HR model output prepared for CMIP6 CMIP piControl, version 20190710.

Krasting, J. P., J. G. John, C. Blanton, C. McHugh, S. Nikonov, A. Radhakrishnan, K. Rand, N. T. Zadeh, V. Balaji, J. Durachta, C. Dupuis, R. Menzel, T. Robinson, S. Underwood, H. Vahlenkamp, K. A. Dunne, P. P. Gauthier, P. Ginoux, S. M. Griffies, R. Hallberg, M. Harrison, W. Hurlin, S. Malyshev, V. Naik, F. Paulot, D. J. Paynter, J. Ploshay, D. M. Schwarzkopf, C. J. Seman, L. Silvers, B. Wyman, Y. Zeng, A. Adcroft, J. P. Dunne, H. Guo, I. M. Held, L. W. Horowitz, P. Milly, E. Shevliakova, C. Stock, M. Winton, and M. Zhao (2018a), NOAA-GFDL GFDL-ESM4 model output prepared for CMIP6 CMIP historical, version 20190726.

Krasting, J. P., J. G. John, C. Blanton, C. McHugh, S. Nikonov, A. Radhakrishnan, K. Rand, N. T. Zadeh, V. Balaji, J. Durachta, C. Dupuis, R. Menzel, T. Robinson, S. Underwood, H. Vahlenkamp, K. A. Dunne, P. P. Gauthier, P. Ginoux, S. M. Griffies, R. Hallberg, M. Harrison, W. Hurlin, S. Malyshev, V. Naik, F. Paulot, D. J. Paynter, J. Ploshay, D. M. Schwarzkopf, C. J. Seman, L. Silvers, B. Wyman, Y. Zeng, A. Adcroft, J. P. Dunne, H. Guo, I. M. Held, L. W. Horowitz, P. Milly, E. Shevliakova, C. Stock, M. Winton, and M. Zhao (2018b), NOAA-GFDL GFDL-ESM4 model output prepared for CMIP6 CMIP piControl, version 20180701.

Lovato, T., and D. Peano (2020a), CMCC CMCC-CM2-SR5 model output prepared for CMIP6 CMIP historical, doi:10.22033/esgf/cmip6.3825.

Lovato, T., and D. Peano (2020b), CMCC CMCC-CM2-SR5 model output prepared for CMIP6 CMIP piControl, doi:10.22033/esgf/cmip6.3874.

NASA-GISS (2018a), NASA-GISS GISS-E2.1G model output prepared for CMIP6 CMIP historical, version 20180827.

NASA-GISS (2018b), NASA-GISS GISS-E2.1G model output prepared for CMIP6 CMIP piControl, version 20180824.

NASA-GISS (2019a), NASA-GISS GISS-E2-1-G-CC model output prepared for CMIP6 CMIP historical, version 20190815.

NASA-GISS (2019b), NASA-GISS GISS-E2-1-G-CC model output prepared for CMIP6 CMIP piControl, version 20190815.

Neubauer, D., S. Ferrachat, C. S.-L. Drian, J. Stoll, D. S. Folini, I. Tegen, K.-H. Wieners, T. Mauritsen, I. Stemmler, S. Barthel, I. Bey, N. Daskalakis, B. Heinold, H. Kokkola, D. Partridge, S. Rast, H. Schmidt, N. Schutgens, T. Stanelle, P. Stier, D. Watson-Parris, and U. Lohmann (2019a), HAMMOZ-Consortium MPI-ESM1.2-HAM model output prepared for CMIP6 CMIP historical, version 20190627.

Neubauer, D., S. Ferrachat, C. S.-L. Drian, J. Stoll, D. S. Folini, I. Tegen, K.-H. Wieners, T. Mauritsen, I. Stemmler, S. Barthel, I. Bey, N. Daskalakis, B. Heinold, H. Kokkola, D. Partridge, S. Rast, H. Schmidt, N. Schutgens, T. Stanelle, P. Stier, D. Watson-Parris, and U. Lohmann (2019b), HAMMOZ-Consortium MPI-ESM1.2-HAM model output prepared for CMIP6 CMIP piControl, version 20190627.

Park, S., and J. Shin (2019a), SNU SAM0-UNICON model output prepared for CMIP6 CMIP historical, version 20190323.

Park, S., and J. Shin (2019b), SNU SAM0-UNICON model output prepared for CMIP6 CMIP piControl, version 20190910.

Ridley, J., M. Menary, T. Kuhlbrodt, M. Andrews, and T. Andrews (2018), MOHC HadGEM3-GC31-LL model output prepared for CMIP6 CMIP piControl, version 20190628.

Ridley, J., M. Menary, T. Kuhlbrodt, M. Andrews, and T. Andrews (2019), MOHC HadGEM3-GC31-LL model output prepared for CMIP6 CMIP historical, version 20190624.

Rong, X. (2019a), CAMS CAMS_CSM1.0 model output prepared for CMIP6 CMIP historical, version 20190708.

Rong, X. (2019b), CAMS CAMS_CSM1.0 model output prepared for CMIP6 CMIP piControl, version 20190729.

Seferian, R. (2018a), CNRM-CERFACS CNRM-ESM2-1 model output prepared for CMIP6 CMIP historical, version 20181206.

Seferian, R. (2018b), CNRM-CERFACS CNRM-ESM2-1 model output prepared for CMIP6 CMIP piControl, version 20181115.

Seland, y., M. Bentsen, D. J. L. Oliviè, T. Toniazzo, A. Gjermundsen, L. S. Graff, J. B. Debernard, A. K. Gupta, Y. He, A. Kirkev, J. Schwinger, J. Tjiputra, K. S. Aas, I. Bethke, Y. Fan, J. Griesfeller, A. Grini, C. Guo, M. Ilicak, I. H. H. Karset, O. A. Landgren, J. Liakka, K. O. Moseid, A. Nummelin, C. Spensberger, H. Tang, Z. Zhang, C. Heinze, T. Iversen, and M. Schulz (2019a), NCC NorESM2-LM model output prepared for CMIP6 CMIP historical, version 20190815.

Seland, y., M. Bentsen, D. J. L. Oliviè, T. Toniazzo, A. Gjermundsen, L. S. Graff, J. B. Debernard, A. K. Gupta, Y. He, A. Kirkev, J. Schwinger, J. Tjiputra, K. S. Aas, I. Bethke, Y. Fan, J. Griesfeller, A. Grini, C. Guo, M. Ilicak, I. H. H. Karset, O. A. Landgren, J. Liakka, K. O. Moseid, A. Nummelin, C. Spensberger, H. Tang, Z. Zhang, C. Heinze, T. Iversen, and M. Schulz (2019b), NCC NorESM2-LM model output prepared for CMIP6 CMIP piControl, version 20190920.

Stouffer, R. (2019a), UA MCM-UA-1-0 model output prepared for CMIP6 CMIP historical, version 20190731.

Stouffer, R. (2019b), UA MCM-UA-1-0 model output prepared for CMIP6 CMIP piControl, version 20190731.

Swart, N. C., J. N. Cole, V. V. Kharin, M. Lazare, J. F. Scinocca, N. P. Gillett, J. Anstey, V. Arora, J. R. Christian, Y. Jiao, W. G. Lee, F. Majaess, O. A. Saenko, C. Seiler, C. Seinen, A. Shao, L. Solheim, K. v. Salzen, D. Yang, B. Winter, and M. Sigmond (2019a), CCCma CanESM5 model output prepared for CMIP6 CMIP historical, version 20190429.

Swart, N. C., J. N. Cole, V. V. Kharin, M. Lazare, J. F. Scinocca, N. P. Gillett, J. Anstey, V. Arora, J. R. Christian, Y. Jiao, W. G. Lee, F. Majaess, O. A. Saenko, C. Seiler, C. Seinen, A. Shao, L. Solheim, K. v. Salzen, D. Yang, B. Winter, and M. Sigmond (2019b), CCCma CanESM5 model output prepared for CMIP6 CMIP piControl, version 20190429.

Swart, N. C., J. N. Cole, V. V. Kharin, M. Lazare, J. F. Scinocca, N. P. Gillett, J. Anstey, V. Arora, J. R. Christian, Y. Jiao, W. G. Lee, F. Majaess, O. A. Saenko, C. Seiler, C. Seinen, A. Shao, L. Solheim, K. v. Salzen, D. Yang, B. Winter, and M. Sigmond (2019c), CCCma CanESM5-CanOE model output prepared for CMIP6 CMIP historical, version 20190429.

Swart, N. C., J. N. Cole, V. V. Kharin, M. Lazare, J. F. Scinocca, N. P. Gillett, J. Anstey, V. Arora, J. R. Christian, Y. Jiao, W. G. Lee, F. Majaess, O. A. Saenko, C. Seiler, C. Seinen, A. Shao, L. Solheim, K. v. Salzen, D. Yang, B. Winter, and M. Sigmond (2019d), CCCma CanESM5-CanOE model output prepared for CMIP6 CMIP piControl, version 20190429.

Tang, Y., S. Rumbold, R. Ellis, D. Kelley, J. Mulcahy, A. Sellar, J. Walton, and C. Jones (2019a), MOHC UKESM1.0-LL model output prepared for CMIP6 CMIP historical, version 20190627.

Tang, Y., S. Rumbold, R. Ellis, D. Kelley, J. Mulcahy, A. Sellar, J. Walton, and C. Jones (2019b), MOHC UKESM1.0-LL model output prepared for CMIP6 CMIP piControl, version 20190827.

Voldoire, A. (2018a), CMIP6 simulations of the CNRM-CERFACS based on CNRM-CM6-1 model for CMIP experiment historical, version 20180917.

Voldoire, A. (2018b), CMIP6 simulations of the CNRM-CERFACS based on CNRM-CM6-1 model for CMIP experiment piControl, version 20180814.

Wieners, K.-H., M. Giorgetta, J. Jungclaus, C. Reick, M. Esch, M. Bittner, S. Legutke, M. Schupfner, F. Wachsmann, V. Gayler, H. Haak, P. d. Vrese, T. Raddatz, T. Mauritsen, J.-S. v. Storch, J. Behrens, V. Brovkin, M. Claussen, T. Crueger, I. Fast, S. Fiedler, S. Hagemann, C. Hohenegger, T. Jahns, S. Kloster, S. Kinne, G. Lasslop, L. Kornblueh, J. Marotzke, D. Matei, K. Meraner, U. Mikolajewicz, K. Modali, W. Müller, J. Nabel, D. Notz, K. Peters, R. Pincus, H. Pohlmann, J. Pongratz, S. Rast, H. Schmidt, R. Schnur, U. Schulzweida, K. Six, B. Stevens, A. Voigt, and E. Roeckner (2019a), MPI-M MPI-ESM1.2-LR model output prepared for CMIP6 CMIP historical, version 20190710.

Wieners, K.-H., M. Giorgetta, J. Jungclaus, C. Reick, M. Esch, M. Bittner, S. Legutke, M. Schupfner, F. Wachsmann, V. Gayler, H. Haak, P. d. Vrese, T. Raddatz, T. Mauritsen, J.-S. v. Storch, J. Behrens, V. Brovkin, M. Claussen, T. Crueger, I. Fast, S. Fiedler, S. Hagemann, C. Hohenegger, T. Jahns, S. Kloster, S. Kinne, G. Lasslop, L. Kornblueh, J. Marotzke, D. Matei, K. Meraner, U. Mikolajewicz, K. Modali, W. Müller, J. Nabel, D. Notz, K. Peters, R. Pincus, H. Pohlmann, J. Pongratz, S. Rast, H. Schmidt, R. Schnur, U. Schulzweida, K. Six, B. Stevens, A. Voigt, and E. Roeckner (2019b), MPI-M MPI-ESM1.2-LR model output prepared for CMIP6 CMIP piControl, version 20190710.

Ziehn, T., M. Chamberlain, A. Lenton, R. Law, R. Bodman, M. Dix, Y. Wang, P. Dobrohotoff, J. Srbinovsky, L. Stevens, P. Vohralik, C. Mackallah, A. Sullivan, S. O'Farrell, and K. Druken (2019a), CSIRO ACCESS-ESM1.5 model output prepared for CMIP6 CMIP historical, version 20191115.

Ziehn, T., M. Chamberlain, A. Lenton, R. Law, R. Bodman, M. Dix, Y. Wang, P. Dobrohotoff, J. Srbinovsky, L. Stevens, P. Vohralik, C. Mackallah, A. Sullivan, S. O'Farrell, and K. Druken (2019b), CSIRO ACCESS-ESM1.5 model output prepared for CMIP6 CMIP piControl, version 20191214.